Journal Name RSCPublishing

ARTICLE

Synthesis and H_2S sensing performance of $MoO_3/Fe_2(MoO_4)_3$ yolk/shell nanostructures†

Cite this: DOI: 10.1039/x0xx00000x

Xinming Gao, Chunyan Li*, Zhuoxun Yin and Yujin Chen*

Received 00th January 2012,
Accepted 00th January 2012

DOI: 10.1039/x0xx00000x

www.rsc.org/

H_2S gas even with a low concentration in environment is very harmful to the health of human beings. Thus, the design and fabrication of gas sensors for detecting trace H_2S gas are highly desirable. Herein we developed a facile method to fabricate $MoO_3/Fe_2(MoO_4)_3$ yolk/shell nanostructures with a porous feature. As the yolk/shell nanostructures were used to fabricate H_2S gas sensors, they exhibited high sensor response, relatively rapid recovery and response times, and good selectivity and long-term stability. The sensor response value of $MoO_3/Fe_2(MoO_4)_3$ yolk/shell nanostructures to 1 ppm H_2S gas was up to 1.7 even at a low working temperature (70°C), significantly higher than those of MoO_3 nanorods and other types of MoO_3 based nanocomposites. Our results demonstrate that the yolk/shell nanostructures have very promising applications in high-performance H_2S sensors.

1 Introduction

With the development of industry, various types of gases are increasingly released into the air, resulting in a serious environmental pollution. Among these gases, H_2S has very harm to the health of human beings and the environment. According to the safety standards established by American Conference of Government Industrial Hygienists, the threshold limit value defined for H_2S is 10 ppm. Therefore, it is very important to develop H_2S gas sensor with a good sensing performance including strong sensor response, rapid response and recovery times, good selectivity and long-term stability.

In the last decades chemical sensors based on metal oxide semiconductors (MOS), such as SnO_2, MoO_3 and In_2O_3 etc.,[1–12] have been extensively investigated due to their low cost, good stability and simplicity in fabricating sensors. However, most of MOS materials had weak response towards H_2S gas even at a high working temperature. Therefore, several approaches, including loading catalyst on the surface of MOS,[13–17] constructing MOS heteronanostructures,[18–29] and doping foreign element in MOS,[30–34] have been developed to improve H_2S sensing performances of MOS materials. As for loading catalyst such as Au, Pt, and Pd on the surface of MOSs, the enhanced sensing mechanism was attributed to greater and faster degree of electron depletion of MOSs.[13–17] However, the introduction of these precious metals would lead to the increase in the costs for sensor fabrications. As for MOS heteronanostructures, their enhanced H_2S sensing performance was related to the change in the heterojunction barrier as the MOSs are exposed to different gases as well as the synergetic effect from different MOS sensing materials. For example, the sensor response of CuO–SnO_2 thin films was up to 4×10^6 toward 50 ppm H_2S at a working temperature of 140°C. The sensing mechanism was attributed to the destruction of p-n junctions formed at the interfaces between SnO_2 and CuO induced by the sulfurization of CuO. However, the thin films exhibited a long recovery time (240 s) due to the slow kinetics of the desulfurization of CuS at 140°C. In addition, the sensing properties of these MOS heteronanostructures are seriously dependent on the sizes of the MOSs and the quality of contacting interfaces.[18–29] As for elemental doping, the doped level and the amount of doped elements in host materials need to be controlled carefully because they had important effects on the sensing properties of MOSs.[30–34]

MOS-based yolk-shell nanostructures have recently attracted great attention because they have potential applications in various fields including electrode materials of lithium-ion battery,[35–39] chemical catalysts,[40] magnetic separation,[41, 42] and drug delivery etc. [43–45] The pore and void space presented in such yolk-shell nanostructures may be in favor of the improvement of their gas sensing performances. However, to the best of our knowledge, the gas sensing properties of the MOS-based yolk-shell nanostructures have been scarcely reported.[46] Herein we report synthesis of $MoO_3/Fe_2(MoO_4)_3$ yolk/shell nanostructures. The materials can detect H_2S gas down to ppm level at a relatively low working temperature. The sensor response value of $MoO_3/Fe_2(MoO_4)_3$ yolk/shell nanostructures to 1 ppm H_2S gas was up to 1.7 even at a low working temperature (70°C), significantly higher than those of MoO_3 nanorods and other types of MoO_3 based nanocomposites. Furthermore, the response and the recovery times of the yolk/shell nanostructrues are only 20 and 70 s, respectively, even at 70°C. In addition, the sensors based the $MoO_3/Fe_2(MoO_4)_3$ yolk/shell nanostructures exhibit good selectivity and long-term stability. Therefore, the yolk/shell nanostructures have very promising applications in high-performance H_2S sensors.

2 Experimental Section

2.1 Synthesis of samples

Single-dispersive MoS_2 spheres were synthesized by a modified hydrothermal method.[47, 48] In a typical experiment, urea (300 mg) was dispersed into ethanol (40 mL) under ultrasonication for 30 min. Then, MoO_3 (15 mg), and thiacetamide (17.5 mg) were added to the suspension under vigorous stirring. After stirring for 1 h, the mixture was then transferred into a Teflonlined stainless steel autoclave with a capacity of 50 mL for hydrothermal treatment at 220°C for 24 h. The autoclave was cooled to room temperature naturally, and then the precipitates were separated by centrifugation, washed with distilled water and absolute ethanol, and dried in a vacuum oven at 40°C for 12 h.

After the single-dispersive MoS_2 spheres were annealed at 500°C for 4 h at air atmosphere, MoO_3 polyhedrons were fabricated. 0.075 g of MoO_3 polyhedrons was dispersed into 300 mL of $Fe(NO_3)_3$ (0.014 mol/L) aqueous solution. The mixture above was kept at 50℃ for 2 h under stirring. The precipitates were separated by centrifugation, washed with distilled water and absolute ethanol, dried under vacuum. The process above was repeatedly carried out for more $Fe(OH)_3$ grown on the MoO_3 polyhedrons.[49] the obtaind sample was named as $MoO_3/Fe(OH)_3$ nanocomposites. $MoO_3/Fe_2(MoO_4)_3$ yolk/shell nanostructures were obtained after $MoO_3/Fe(OH)_3$ nanocomposites were annealed at 500°C for 4 h at air atmosphere.

2.2 Analysis techniques

The morphology and microstructure of the samples were characterized by scanning electron microscopy (SEM, JEOL-JSM-6700F), and transmission electron microscope (TEM, JEOL 2010). The compositional analysis was carried out using an energy dispersive spectroscopy (EDS) setup attached to the SEM. The crystal structures were measured by X-ray diffraction (XRD, Cu Kα radiation) using D/Max–TTR III diffractometer.

2.3 Fabrication of gas sensor and the sensing measurements

The fabrication and testing principle of the gas sensor are similar to those described in our previous reports.[50] Simply, the sample was dissolved in absolute ethanol, and a drop was spun on a ceramic tube between metal electrodes to form a thin film with a thickness of about 0.1 mm. A metal alloy coil through the ceramic tube was used to control the working temperature of the gas sensor. Scheme 1(a) illustrates the configuration of the sensor. The gas sensing properties were tested by ZWS1-WS-30A system (Zhongxi yuanda Science and Technology Co., Ltd., China) with a test chamber of 18 L, a gas-intake window, 30 testing channels, and temperature controlled system. Figure S1 in ESI shows the photograph of the measurement set up.†The standard tested gases were purchased from Beijing Kshergas Co., Ltd., China. A stationary state gas distribution method was used for testing the gas sensing properties. The sensor was placed in a test chamber full of fresh air at the beginning, and then a given amount of test gas was injected into the chamber by an injector. After the response reaching a steady value, the sensor was exposed to ambient environment by opening the chamber. Detected gases such as H_2S were injected into the test chamber and mixed with air. The gas concentration was calculated according to the ideal gas equation. Scheme 1(b) illustrates the measuring principle for determining the sensor response. R_l denotes a constant load resistor, R_g the resistance of the nanotubes which can be adjusted at different gas molecule atmosphere. The voltage drop (V_l) across the resistor (R_l) can be measured by a voltmeter. Thus, the sensor response of the nanotubes can be calculated based on the measured data above. The sensor response was measured repeatedly by five times. The sensing properties of the H_2S gas sensors were measured under atmosphere conditions with a relative humidity of 19% and ambient temperature of 25℃. The sensor response (S) is defined as $S=R_a/R_g$, where R_a is the sensor resistance in air and R_g is the resistance in target-air mixed gas, respectively. The response and recovery times were defined as the time needed for 90% of total resistance change after the sensor was exposed to the tested gas and air, respectively.

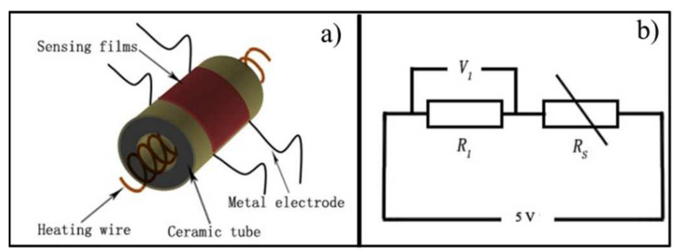

Scheme 1 Illustrations of the sensor configuration and the measuring principle for determining the sensor response.

3 Results and discussion

3.1 Structure characterization of samples

SEM images (Figure 1(a)) show that single-dispersive MoS_2 spheres can be obtained through the present method. The diameter of the uniform and single-dispersive MoS_2 spheres is about 500 nm. After the heating of MoS_2 spheres at 500°C for 4 h at air atmosphere, MoO_3 with an irregular polyhedron-like morphology were obtained (Figure S2, ESI).† XRD peaks of the product (Figure 2(a)) can be indexed to orthorhombic MoO_3 (JCPDs card number 35-0609; space group *pbnm*(62), orthorhombic symmetry with lattice constants a = 0.3963 nm, b = 1.3856 nm and c = 0.3697 nm). The intensity of the diffraction peak of (021) plane is higher than that of corresponding (040) plane, indicating the anisotropic growth of the MoO_3 polyhedrons in (0kl) planes.[11, 34] No other diffraction peaks are detected, indicating a high crystal purity of MoO_3 polyhedrons. The SEM image (Figure 1(b)) displays the average length and thickness of MoO_3 polyhedrons are about 240 and 80 nm, respectively. The transformation of MoS_2 to MoO_3 is due to the oxidization of MoS_2 at a high temperature under ambient atmosphere, as described by Equation 1. During the transformation process the crystalline structures were changed, leading to the different morphologies of the samples before and after the transformation.

$$2MoS_2 + 7O_2 \rightarrow 2MoO_3 + 4SO_2 \quad (1)$$

Figure 1(c) is a typical SEM image of $MoO_3/Fe(OH)_3$ nanocomposites. It can be found that many $Fe(OH)_3$ nanosheets were grown on the surfaces of MoO_3 polyhedrons. The length of the $MoO_3/Fe(OH)_3$ nanocomposites is in range of 250-850 nm. Similar to the previous results,[9, 23] $Fe(OH)_3$ is amorphous, which evidenced by the selected area electron diffraction (SAED) measurements. In the SAED pattern (Figure 1(d)), only diffraction spots coming from MoO_3 can be observed. There are not the diffraction peaks from other materials except those from MoO_3 in XRD pattern (Figure 2(b)), which further confirms that $Fe(OH)_3$ is amorphous. Notably, no obvious change in the relative intensities of the diffraction peaks is observed, suggesting similar predominant direction growth of MoO_3 in the composite to that of the initial MoO_3 polyhedrons.[11, 34]

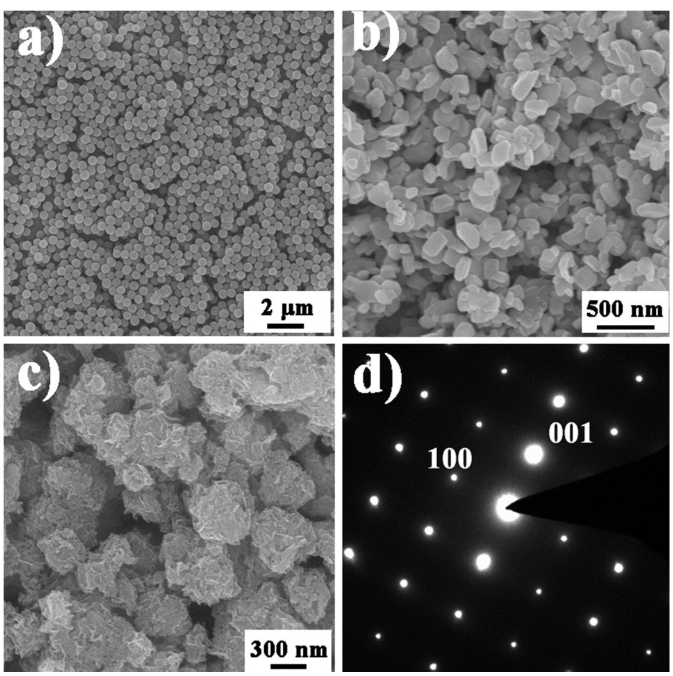

Figure 1 a) SEM image of single-dispersive MoS_2 spheres, b) SEM image of MoO_3 polyhedrons, c) SEM image of $MoO_3/Fe(OH)_3$ nanocomposites, and d) SAED pattern of $MoO_3/Fe(OH)_3$ nanocomposites.

After $MoO_3/Fe(OH)_3$ nanocomposites were annealed at 500°C for 4 h at air atmosphere, $MoO_3/Fe_2(MoO_4)_3$ yolk/shell nanostructures were then obtained. Figure 2(c) shows XRD pattern of $MoO_3/Fe_2(MoO_4)_3$ yolk/shell nanostructures. All the peaks marked by the Miller indices in Figure 2(c) can be indexed to the monoclinic $Fe_2(MoO_4)_3$ (JCPDS card number 83-1701, cell parameters: a = 15.70 Å, b = 9.231 Å, c= 18.20 Å, β=125.2°). Besides, the peaks labeled by the black frames come from (021), (041), (061) and (081) planes of orthorhombic MoO_3, respectively. The results above reveal that the yolk/shell nanostructures consist of crystalline $Fe_2(MoO_4)_3$ and MoO_3. Notably, the intensities of the diffraction peaks of (0k0) planes of MoO_3 in the yolk/shell nanostructures are relatively weak. On one hand, it shows no change in its predominant direction after the annealing process; on the other hand, it reveals that the content of MoO_3 in the yolk/shell nanostructures is smaller than that of $Fe_2(MoO_4)_3$. According to the Scherrer equation the calculated the crystal size of $Fe_2(MoO_4)_3$ crystals in the yolk/shell nanostructures is 36.4 nm. EDS analyses are conducted to determine the compositional content of the yolk/shell nanostructure, as shown in Figure S3.† Statistical results show that the atomic ratio of Fe to Mo is aroud 1: 1.93, and thereby the content of $Fe_2(MoO_4)_3$ in the yolk/shell nanostructures is about 90.53 wt%.

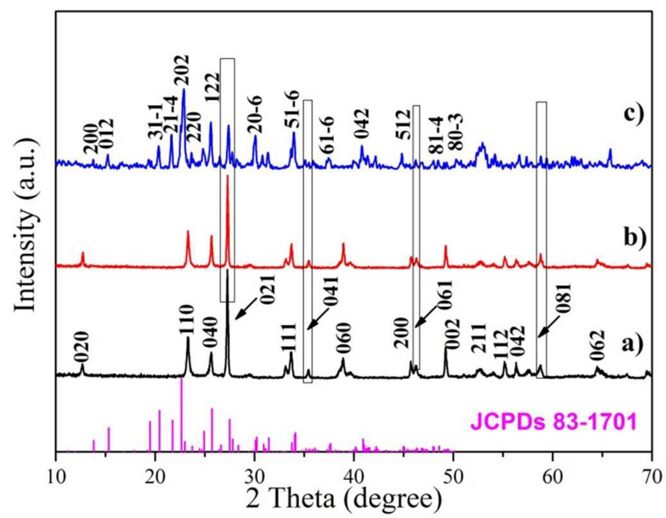

Figure 2 XRD patterns of a) MoO_3 polyhedrons, b) $MoO_3/Fe(OH)_3$ nanocomposites, and c) $MoO_3/Fe_2(MoO_4)_3$ yolk/shell nanostructures. The peaks highlighted by the black frames display no obvious change in the predominant growth of MoO_3 in (0kl) in different samples.

The morphology and the structure of $MoO_3/Fe_2(MoO_4)_3$ yolk/shell nanostructures were investigated by SEM and TEM analyses. Figure 3(a) shows a typical SEM image of the product. It can be seen that $MoO_3/Fe_2(MoO_4)_3$ yolk/shell nanostructures have similar morphologies and size to those of $MoO_3/Fe(OH)_3$ nanocomposites. TEM image (Figure 3(b)) reveals that the product exhibits a character of yolk/shell structure. In the SAED pattern, besides the diffraction spots from MoO_3, the diffraction rings attributed to $Fe_2(MoO_4)_3$ can be observed. This further confirms that the product is composed of crystalline $Fe_2(MoO_4)_3$ and MoO_3. The spacing labeled in the HRTEM image taken from the outside region of the nanostructures is about 0.287 nm, corresponding to (024) crystal plane of $Fe_2(MoO_4)_3$. In addition, in the HRTEM image many white spots can be observed, suggesting there are small pores in the yolk/shell nanostructures. The results above suggest that $Fe(OH)_3$ and part of MoO_3 are transformed into $Fe_2(MoO_4)_3$. The transformation process is similar to one based on the nanoscale Kirkendall effect which usually used to fabricate hollow inorganic nanocrystals.[51] At a temperature above 100°C, $Fe(OH)_3$ is transformed into Fe_2O_3 gradually. At a high temperature, MoO_3 diffused outward and reacted with Fe_2O_3, and then $Fe_2(MoO_4)_3$ gradually produced. Because MoO_3 diffused outward faster than Fe_2O_3 did inward, the void spaces would be left in the inner of the nanostructures. Finally, the yolk/shell nanostructures are formed.

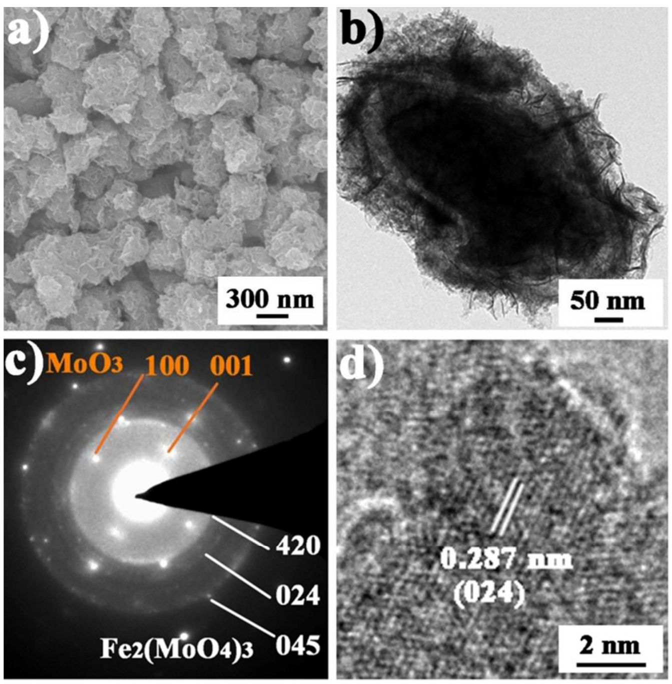

Figure 3 Structural characterization of $MoO_3/Fe_2(MoO_4)_3$ yolk/shell nanostructures. a) SEM image, b) TEM image, c) SAED pattern, and d) HRTEM image.

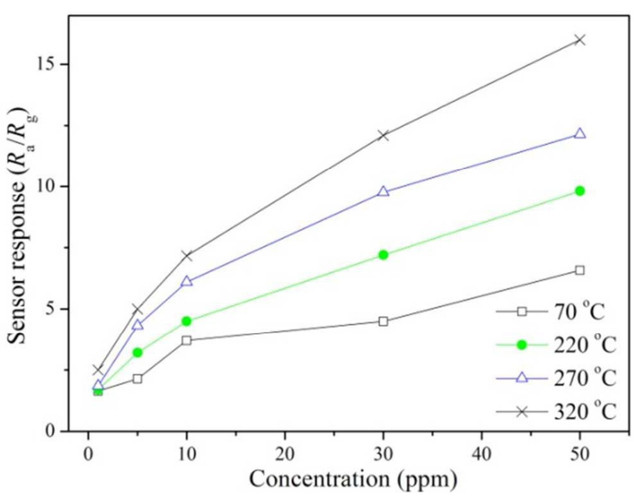

Figure 4 Sensor responses of $MoO_3/Fe_2(MoO_4)_3$ yolk/shell nanostructures to H_2S gases with different concentrations at various working temperatures.

3.2 gas sensing performances of $MoO_3/Fe_2(MoO_4)_3$ yolk/shell nanostructures

Because the $MoO_3/Fe_2(MoO_4)_3$ yolk/shell nanostructures have similar structural character to that of the hollow nanostructures, they may show good gas sensing performances.[52] Figure 4 shows sensor responses of $MoO_3/Fe_2(MoO_4)_3$ yolk/shell nanostructures to H_2S gas with different concentrations at various working temperatures. It can be found that the $MoO_3/Fe_2(MoO_4)_3$ yolk/shell nanostructures have very close sensor response to 1 ppm H_2S gas at all the tested temperatures, but the sensor responses to H_2S with a concentration of higher than 5 ppm increase with the increase of the working temperature. It may be related to the sensing mechanism of the yolk/shell nanostructures, which will be discussed later. The sensor response value of the $MoO_3/Fe_2(MoO_4)_3$ yolk/shell nanostructures to 1 ppm H_2S gas is about 1.7 at a working temperature of 70°C, greatly higher than those of other sensing materials.[9, 23, 24] For example, MoO_3 nanorods and MoO_3/ZnO cage-like nanocomposites have almost no response to 5 ppm H_2S gas at a working temperature of 80°C.

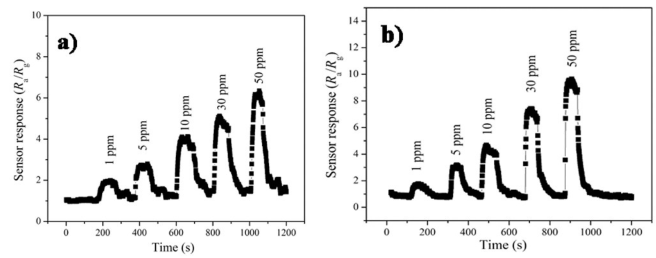

Figure 5 Time-dependent sensor responses of $MoO_3/Fe_2(MoO_4)_3$ yolk/shell nanostructures at various working temperatures. a) 70°C, and b) 220°C.

The enhanced sensing performance of the $MoO_3/Fe_2(MoO_4)_3$ yolk/shell nanostructures may be related to their sensing mechanisms. Previous results reported by Illyaskutty et al showed that unlike to other metal oxide semiconductors such as SnO_2, the gas detection process with MoO_3 mainly directed by the surface lattice oxygen (oxygen vacancy in MoO_3) rather than the chemisorbed oxygen.[11, 34, 53] Lattice oxygen from MoO_3 the surface layer catalytically oxidized the analyte gas, and it was simultaneously reduced, which determined the change in conductivity. Therefore, MoO_3 exhibited good sensing performance towards reducing gases such as ethanol and H_2S. On the other hand, $Fe_2(MoO_4)_3$ is also a kind of oxidation catalyst.[54, 55] Thus, the synergistic effect may be attributed to the enhanced sensing performance of the $MoO_3/Fe_2(MoO_4)_3$ yolk/shell nanostructures. The catalytic ability of MoO_3 can be improved by the increase of the temperature, leading to the increase of sensor response with increase of the working temperature.[11, 34, 53] Furthermore, $Fe_2(MoO_4)_3$ exhibited strong catalytic properties even at a temperature below 160°C,[54, 55] whereas MoO_3 had sensor response toward ethanol vapor at a temperature above 200°C.[11, 34] In the present work, the content of $Fe_2(MoO_4)_3$ is greatly higher than that of MoO_3, leading to the enhanced sensing performance of the $MoO_3/Fe_2(MoO_4)_3$ yolk/shell nanostructures compared to pure MoO_3 material.[23] In addition, The $MoO_3/Fe_2(MoO_4)_3$ yolk/shell nanostructures have small pores, as shown in Figure 3(b). The small pores allow more gas molecules to diffuse into/outward the sensing material layers effectively. Moreover, the pores can act as active sensing sites, which offer additional advantages of high sensitivity.[11, 34, 53]

To further investigate the H_2S sensing performances of the $MoO_3/Fe_2(MoO_4)_3$ yolk/shell nanostructures, we also measured their time-dependent responses to H_2S gases with different concentrations. The response and recovery times were defined as the time needed for 90% total resistances change after the sensor exposed to the tested gas and air, respectively. Figure 5(a) shows the response and recovery times of the $MoO_3/Fe_2(MoO_4)_3$ yolk/shell nanostructures at 70°C are about 20 and 70 s, respectively. The recovery time at the temperature is relatively long, but it can be decreased if the working temperature is increased. For example, the recovery time decreases to about 25 s as the working temperature is increased to 220°C, as shown in Figure 5(b).

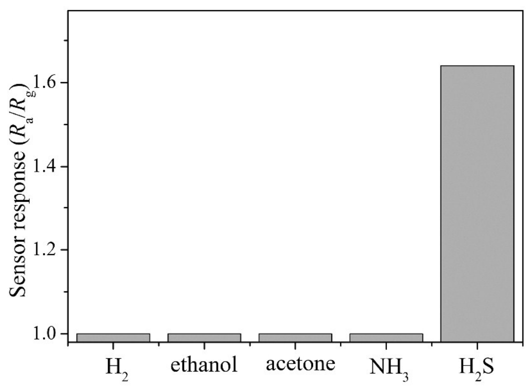

Figure 6 Selectivity of $MoO_3/Fe_2(MoO_4)_3$ yolk/shell nanostructures. The working temperature is 70°C and the concentrations of all detected gases are 1 ppm.

The gas sensors for practical applications are required not only to have strong sensor response, and quick response time and recovery time, but also to have very good selectivity to the targeted gas. Therefore, the sensor responses of the $MoO_3/Fe_2(MoO_4)_3$ yolk/shell nanostructures to 1 ppm H_2, ethanol vapor, acetone, and NH_3 at 70°C were measured to evaluate their selectivity. As shown in Figure 6, the $MoO_3/Fe_2(MoO_4)_3$ yolk/shell nanostructures have almost no responses to those gases at the working temperature. It reveals that the $MoO_3/Fe_2(MoO_4)_3$ yolk/shell nanostructures have good selectivity to H_2S gas. It may be related to the different surface reaction dynamics of the yolk/shell for different gases. For example, Pd/ZnO sensors have excellent selectivity to ethanol.[56] In addition, the gas concentration has an effect on the sensor response. For example, the sensor responses of the yolk/shell nanostructures to 100 ppm ethanol and H_2S are 5.0 and 8.6, respectively, as shown in Figure S4.† The long-term stability of the yolk/shell nanostructures was also measured. As shown in Figure 7, The sensor responses of the yolk/shell nanostructures to 1 ppm H_2S at 70°C are kept almost the same values for 60 days of testing, suggesting they have a good stability as they are used as H_2S gas sensors. The high sensor response, relatively rapid recovery and response times, good selectivity and stability of the yolk/shell nanostructures demonstrate that they have very promising applications in H_2S gas sensors.

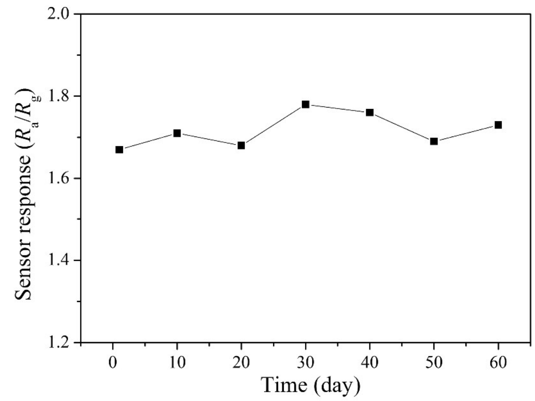

Figure 7 Stability of $MoO_3/Fe_2(MoO_4)_3$ yolk/shell nanostructures as H_2S sensors. The working temperature is 70°C and the concentration of detected H_2S gas is 1 ppm.

4 Conclusions

In summary, the $MoO_3/Fe_2(MoO_4)_3$ yolk/shell nanostructures with a porous feature were successfully fabricated by a facile method. As the yolk/shell nanostructures used as H_2S gas sensors, they exhibited high sensor response, relatively rapid recovery and response times, good selectivity and stability. Importantly, the $MoO_3/Fe_2(MoO_4)_3$ yolk/shell nanostructures could detect 1 ppm H_2S gas at a relatively working temperature (70°C). Furthermore, compared to pure MoO_3 and some MoO_3-based sensing materials, the yolk/shell nanostructures exhibited enhanced H_2S sensing properties, which can be attributed to the synergistic effect of MoO_3 and $Fe_2(MoO_4)_3$ and the porous feature of the yolk/shell nanostructures. Our results indicate that the yolk/shell nanostructures are good candidates for high-performance H_2S sensors.

Acknowledgements

We thank the National Natural Science Foundation of China (Grant Nos. 51272050 and 21271053), the Innovation Foundation of Harbin City (2012RFXXG096), and also the 111 project (B13015) of Ministry Education of China to the Harbin Engineering University.

Notes and references

Key Laboratory of In-Fiber Intregrated Optics, Ministry of Education, and College of Science, Harbin Engineering University, Harbin 150001, China. Fax: 86-451-82519754; Tel: 86-451-82519754; E-mail: chenyujin@hrbeu.edu.cn and chunyanli@hrbeu.edu.cn

†Electronic Supplementary Information (ESI) available: [The measurement set up for gas sensor, high-resolution SEM image of MoO_3 polyhedrons, EDS pattern of the yolk/shell nanostructures and sensor responses of the yolk/shell nanostructures to different kinds of gases with a concentrition of 100 ppm]. See DOI: 10.1039/c000000x/

1 Y. J. Chen, C. L. Zhu and G. Xiao, *Sens. Actuators B*, 2008, **129**, 639–642.

2 Z. L. Zhan, J. W. Lu, W.H. Song, D. G. Jiang and J. Q. Xu, *Mater. Res. Bull.*, 2007, **42**, 228–235.
3 H.-J. Kim and J.-H. Lee, *Sens. Actuators B*, 2014, **192**, 607–627.
4 R. Ionescu, A. Hoel, C. G. Granqvist, E. Llobet and P. Heszler, , *Sens. Actuators B*, 2005, **104**, 132–139.
5 G. S. Devi, S. Manorama and V. J. Rao, *Sens. Actuators B*, 1995, **28**, 31–37.
6 D. Calestani, M. Zha, R. Mosca, A. Zappettini, M. C. Carotta, V. D. Natale and L. Zanotti, *Sens. Actuators B*, 2010,**144**, 472–478.
7 J. L. Solis, S. Saukko, L. B. Kish, C. G. Granqvist and V. Lantto, *Sens. Actuators B*, 2001, **77**, 316–321.
8 A. Katoch, J. -H. Byun, S. -W. Choi and S. S. Kim, *Sens. Actuators B*, 2014, **202**, 38–45.
9 Y. J. Chen, X. M. Gao, X. P. Di, Q. Y. Ouyang, P. Gao, L. H. Qi, C. Y. Li and C. L. Zhu, *ACS Appl. Mater. Interfaces*, 2013, **5**, 3267–3274.
10 Y. J. Chen, F. N. Meng, H. L. Yu, C. L. Zhu, T. S. Wang, P. Gao and Q. Y. Ouyang, *Sens. Actuators B*, 2013, **176**, 15–21.
11 N. Illyaskutty, H. Kohler, T. Trautmann, M. Schwotzer and V. P. M. Pillai, *Sens. Actuators B*, 2013, **187**, 611–621.
12 O. Lupan, V. Cretu, M. Deng, D. Gedamu, I. Paulowicz, S. Kaps, Y. K. Mishra, O. Polonskyi, C. Zamponi, L. Kienle, V. Trofim, I. Tiginyanu and R. Adelung, *J. Phys. Chem. C*, 2014, **118**, 15068–15078.
13 A. Kolmakov, D. O. Klenov, Y. Lilach, S. Stemmer and M. Moskovits, *Nano Lett.*, 2005, **5**, 667–673.
14 N. S. Ramgir, P. K. Sharma, N. Datta, M. Kaur, A. K. Debnath, D. K. Aswal and S. K. Gupta, *Sens. Actuators B*, 2013, **186**,718–726.
15 S. -W. Tsai and J. -C. Chiou, *Sens. Actuators B*, 2011, **152**, 176–182.
16 Y. B. Shen, B. Q. Zhang, X. M. Cao, D. Z. Wei, J. W. Ma, L. J. Jia, S. L. Gao, B. Y. Cui and Y. C. Jin, *Sens. Actuators B*, 2014, **193**, 273–279.
17 H. Kim, C. Jin, S. Park, S. Kim and C. Lee, *Sens. Actuators B*, 2012, **161**, 594–599.
18 K. Choi, H. -J. Kim, Y. C. Kang and J. -H. Lee, *Sens. Actuators B*, 2014, **194**, 371–376.
19 S. -W. Choi, J. Zhang, K. Akash and S. S. Kim, *Sens. Actuators B*, 2012, **169**, 54–60.
20 S. -W. Choi, A. Katoch, J. Zhang and S. S. Kim, *Sens. Actuators B*, 2013, **176**, 585–591.
21 F. Shao, M. W. G. Hoffmann, J. D. Prades, R. Zamani, J. Arbiol, J. R. Morante, E. Varechkina, M. Rumyantseva, A. Gaskov, I. Giebelhaus, T. Fischer, S. Mathur and F. Hernández-Ramírez, *Sens. Actuators B*, 2013, **181**, 130–135.
22 Y. J. Chen, F. N. Meng, C. Ma, W. Yang, C. L. Zhu, Q. Y. Ouyang, P. Gao, J. Q. Li and C. W. Sun, *J. Mater. Chem.*, 2012, **22**, 12900–12906.
23 H. L. Yu, L. Li, X. M. Gao, Y. Zhang, F. N. Meng, T. S. Wang, G. Xiao, Y. J. Chen and C.L. Zhu, *Sens. Actuators B*, 2012, **171–172**, 679–685.
24 C. L. Zhu, H. L. Yu, Y. Zhang, T. S. Wang, Q. Y. Ouyang, L. H. Qi, Y. J. Chen and X. Y. Xue, *ACS Appl. Mater. Interfaces*, 2012, **4**, 665–671.
25 T. S. Wang, Q. S. Wang, C. L. Zhu, Q. Y. Ouyang, L. H. Qi, C. Y. Li, G. Xiao, P. Gao and Y. J. Chen, *Sens. Actuators B*, 2012, **171–172**, 256–262.
26 F. N. Meng, X. P. Di, H. W. Dong, Y. Zhang, C. L. Zhu, C. Y. Li and Y. J. Chen, *Sens. Actuators B*, 2013, **182**, 197–204.
27 A. Khanna, R. Kumar and S. S. Bhatti, *Appl. Phys. Lett.*, 2013, **82**, 4388.
28 A. Chowdhuri, V. Gupta, K. Sreenivas, R. Kumar and S. Mozumdar and P. K. Patanjali, *Appl. Phys. Lett.*, 2013, **84**, 1180.
29 X. Y. Xue, L. L. Xing, Y. J. Chen, S. L. Shi, Y. G. Wang and T. H. Wang, *J. Phys. Chem. C* 2008, **112***,* 12157–12160.
30 J. Liu, W. Guo, F. Qu, C. Feng, C. Li, L. Zhu, J. Zhou, S. Ruan and W. Chen, *Ceram. Int.*, 2014, **40**, 6685–6689.
31 M. G. Zhao, X. C. Wang, L. L. Ning, J. F. Jia, X. J. Li and L. L. Cao, *Sens. Actuators B*, 2011, **156**, 588–592.
32 P. S. Shewale, V. B. Patil, S. W. Shin, J. H. Kim and M. D. Uplane, *Sens. Actuators B*, 2013, **186**, 226–234.
33 Q. Y. Ouyang, L. Li, Q. S. Wang, Y. Zhang, T. S. Wang, F. N. Meng, Y. J. Chen and P. Gao, *Sens. Actuators B*, 2012, **169**, 17–25.
34 N. Illyaskutty, H. Kohler, T. Trautmann, M. Schwotzer and V. P. M. Pillai, *J. Mater. Chem.C*, 2013, **1**, 3976–3984.
35 S. H. Choi and Y. C. Kang, ACS Appl. Mater. Interfaces, 2014, **6**, 2310–2314.
36 J. X. Wang, W. Li, F. Wang, Y. Y. Xia, A. M. Asiri and D. Y. Zhao, *Nanoscale*, 2014, **6**, 3217–3222.
37 Y. J. Hong, M. Y. Son and Y. C. Kang, *Adv. Mater.*, 2013, **25**, 2279–2283.
38 M. Y. Son, Y. J. Hong, J. -K. Lee and Y. C. Kang, *Nanoscale*, 2013, **5**, 11592–1159.
39 H. C. Pang, P. Cheng, H. B. Yang, J. L. Liu, C. X. Guo, G. L. Ning and C. M. Li, *Chem. Commun.*, 2013, **49**, 1536–1538.
40 Y. X. Ye, L. Kuai and B. Y. Geng, *J. Mater. Chem.*, 2012, **22**, 19132–19138.
41 X. Q. Zhang, H. Ren and T. T. Wang, *J. Mater. Chem.*, 2012, **22**, 13380–13385.
42 S. H. Kim, Y. D. Yin, A. P. Alivisatos, G. A. Somorjai, J. T. Yates and Jr., *J. Am. Chem. Soc.*, 2007, **129**, 9510–9513.
43 Q. L. Fang, S. H. Xuan, W. Q. Jian and X. L. Gong, *Adv. Funct. Mater.*, 2011, **21**, 1902–1909.
44 J. Liu, S. Z. Qiao, J. S. Chen, X. W. Lou, X. R. Xing and G Q. Lu, *Chem. Commun.*, 2011, **47**, 12578–12591.
45 J. H. Gao, G. L. Liang, B. Zhang, Y. Kuang, X. X. Zhang and B. Xu, *J. Am. Chem. Soc.*, 2007, **129**, 1428–1433.
46 Y. J. Hong, J. -W. Yoon, J. -H. Lee, Y. C. Kang, *Chem. Eur. J.*, 2014, **20**, 2737–2741.
47 H. L. Yu, C. Ma, B. H. Ge, Y. J. Chen, Z. Xu, C. L. Zhu, C. Y. Li, Q. Y. Ouyang, P. Gao, J. Q. Li, C. Sun, L. H. Qi, Y. M. Wang and F. H. Li, *Chem. Eur. J.*, 2013, **19**, 5818–5823.
48 H. L. Yu, C. L. Zhu, K. Zhang, Y. J. Chen, C. Y. Li, P. Gao, P. P. Yang and Q. Y. Ouyang, *J. Mater. Chem. A*, 2014, **2**, 4551–4557.
49 Y. L. Ren, H. Y. Wu, M. M. Lu, Y. J. Chen, C. L. Zhu, P. Gao, M. S. Cao, C. Y. Li and Q. Y. Ouyang, *ACS Appl. Mater. Interfaces*, 2012, **4**, 6436–6442.
50 Y. J. Chen, G. Xiao, T. S. Wang, F. Zhang, Y. Ma, P. Gao, C. L. Zhu, E. D. Zhang, Z. Xu and Q. H. Li**,** *Sens. Actuators B*, 2011, **156**, 867–874.
51 Y. Yin, R. M. Rioux, C. K. Erdonmez, S. Hughes, G. A. Somorjai and A. P. Alivisatos, *Science*, 2004, **304**, 711–714.
52 J. H. Lee, *Sens. Actuators B,* 2009, **140**, 319–336.
53 N. Illyaskutty, S. Sreedhar, H. Kohler, R. Philip, V. Rajan and V.P. M. Pilai, *J. Phys. Chem. C* 2013, **117**, 7818–7829.
54 M. P. House, A. F. Carley, R. Echeverria-Valda and M. Bowker, *J. Phys. Chem. C*, 2008, 112, 4333–341.
55 L. Wang, B. Peng, X. F. Guo, W. P. Ding and Y. Chen, *Chem Commun.*, 2009, 1565–1567.
56 Y. Zhang, Q. Xiang, J. Q. Xu, P. C. Xu, Q. Pan and F. Li, *J. Mater.Chem.*, 2009, 19, 4701–4706.

A facile method was developed to fabricate $MoO_3/Fe_2(MoO_4)_3$ yolk/shell nanostructures with small pores, exhibiting good H_2S gas sensing performance including high sensor response, short recovery and response times, and good selectivity and stability.